Nanoscale

Accepted Manuscript

Volume 10
Number 4
28 January 2018
Pages 1549-2172

Nanoscale

rsc.li/nanoscale

ISSN 2040-3372

PAPER
Shuping Xu, Chongyang Liang *et al.*
Organelle-targeting surface-enhanced Raman scattering (SERS) nanosensors for subcellular pH sensing

ROYAL SOCIETY OF CHEMISTRY

NCNST

This is an Accepted Manuscript, which has been through the Royal Society of Chemistry peer review process and has been accepted for publication.

Accepted Manuscripts are published online shortly after acceptance, before technical editing, formatting and proof reading. Using this free service, authors can make their results available to the community, in citable form, before we publish the edited article. We will replace this Accepted Manuscript with the edited and formatted Advance Article as soon as it is available.

You can find more information about Accepted Manuscripts in the Information for Authors.

ROYAL SOCIETY OF CHEMISTRY

rsc.li/nanoscale

ARTICLE

Deterministic Fabrication of Highly Reproducible Monochromatic Quantum Emitters in Hexagonal Boron Nitride

Muchuan Hua[1], Wei-Ying Chen[2], Hanyu Hou[1,3], Venkata Surya Chaitanya Kolluru[1], Maria K. Y. Chan[1], Haihua Liu[1], Thomas E. Gage[1]*, Jian-Min Zuo[3]*, Benjamin T. Diroll[1]*, Jianguo Wen[1]*

Quantum emitters in hexagonal boron nitride are important room temperature single photon sources. However, conventional fabrication methods yield quantum emitters with dispersed and inconsistent spectral profiles, limiting their potential for practical quantum applications, which demands reproducible high quality single photon sources. Here, the authors report deterministic creation of highly reproducible monochromatic quantum emitters by applying carbon-ion implantation on freestanding hexagonal boron nitride flakes, while a carbon mask with suitable thickness was adapted to optimize the implantation results. Quantum emitters fabricated using this approach exhibited thermally limited monochromaticity, with an emission center wavelength of 590.7 ± 2.7 nm, a narrow full width half maximum of 7.1 ± 1.7 nm, an emission rate of 1 MHz without optical engineering, and exceptional stability under ambient conditions. Density functional theory calculations and scanning transmission electron microscopy suggest that these emitters are comprised of boron centered carbon tetramers. This method provides a reliable single photon source for optical quantum computing and potential future industry-scale applications.

Introduction

Quantum information science (QIS) is an emerging field at the intersection of quantum physics, computer science, and information theory. It uses the basic rules of quantum mechanics to handle and process information in ways that traditional computing cannot match. Various materials and devices are being actively investigated as platform technologies for QIS [1–7], with photon-based quantum information processing, communication, and transduction emerging as key areas within the field. These photon-based systems provide distinct advantages, including long-lived quantum states, minimal environmental interference, and the capability to transmit quantum information over long distances through optical fibers [8–11]. The essential component of these systems is a quantum emitter (QE) that can stably produce indistinguishable single photons at a high emission rate, and many efforts has been investigated in QE fabrication upon difference materials and platform [12–15].

Two-dimensional (2D) materials, such as transition metal dichalcogenides and hexagonal boron nitride (hBN), have been found to be possible hosts for QEs, attracting significant research interest in the last decade [16–22]. In particular, hBN has been extensively studied for QE creation as its large electronic band gap and optical phonon energy, in principle, allow it to host QEs at room temperature with perfect monochromaticity [23–28]. Existing approaches have successfully achieved spatial control in the creation of QEs, however, most of them have limited control of the QEs' spectral properties (random emission wavelength with broad intensity profile), limiting practical use. Recently, both theoretical and experimental works have suggested that carbon related defects are a major source of the visible (from 435 nm to 700 nm) QEs in hBN [20,29–37]. Thus, an improved carbon implantation method for hBN with controlled defect creation is valuable not only for improving the generated QEs' repeatability and quality, but also for significantly reducing the complexity in identifying correlations between defect atomic structures and observed single-photon emission behaviors.

In this study, we report a deterministic QE creation for freestanding hBN flakes through masked-carbon-ion-implantation (MCI) yielding two types of room temperature QEs with reproducible atom-like emission profiles. The QEs created

[1.] Center for Nanoscale Materials, Argonne National Laboratory, 9700 S. Cass Avenue, Lemont, 60439, Illinois, the United States.

[2.] Nuclear Science and Engineering, Argonne National Laboratory, 9700 S. Cass Avenue, Lemont, 60439, Illinois, the United States.

[3.] Materials Science & Engineering, University of Illinois Urbana Champaign, 1304 W. Green St. MC 246, Urbana, 61801, Illinois, the United States.

*Corresponding authors

using this process have remarkable monochromaticity with a standard deviation of 2.5 nm in zero phonon line (ZPL) wavelengths, and a typical full-width-half-maximum (FWHM) under 25 meV at room temperature. In addition to single-photon behaviors, they are also exceptionally stable (no observable degradation after days with 10^5 W/cm^2 laser excitation) and bright (1 MHz emission rate). With the help of first principles density functional theory defect calculations and scanning transmission electron microscopy, the QEs were determined as radical carbon tetramers centered at boron sites.

Results and Discussion

To achieve more consistent creation of carbonaceous defects in hBN with desired optical properties, typical ion bombardment procedures were modified to minimize lattice damage and generate defects in the middle of the hBN flake. This was achieved by employing an amorphous carbon mask, placed in front of the freestanding hBN flake to decelerate incoming carbon ions (Fig. 1a). The masks were designed and fabricated with a thickness that ensures the carbon ions most probable penetration depth aligns with the middle of the hBN flake, for example, a 100 nm thick carbon mask was used for a 16 monolayer hBN flake (Fig. 1b) to achieve the maximum stopping efficiency of carbon ions [38]. Such configuration maximized the doping efficiency, leaving less damage due to other defects such as vacancies (detailed in SI). Meanwhile, typical contamination caused by the recoiling of the mask elements was automatically precluded as the mask and the implantation ions were made of the same element. The authors note that reducing the ion acceleration energy could also lead to shallower implantation depths, potentially eliminating the need for a carbon mask.
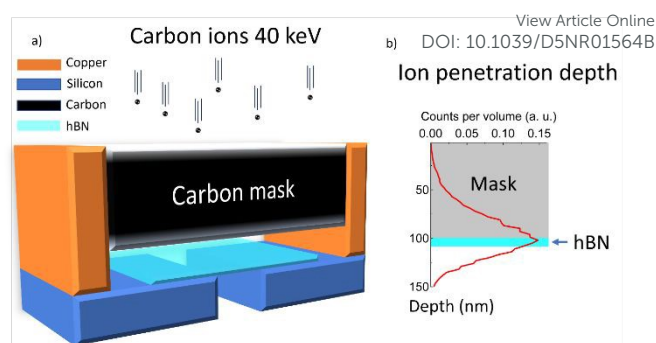

Fig. 1(a) Scheme of the masked-carbon-ion implantation process. (b) Simulated penetration depth of the carbon ions (curve obtained with 100nm carbon mask and 5nm thick hBN flake.

However, the IVEM-Tandem facility used in this study currently supports a minimum energy of 40 kV. To minimize the intrinsic defects of the sample, for instance the defects created during the synthesis, hBN flakes exfoliated from high-quality pristine crystal bulk were used. Since previous work on optical properties of the QEs created by carbon-ion-implantation have found strong substrate dependence [31], in this research, the hBN flakes were stamped on to Si or SiN transmission electron microscopy (TEM) grids with pre-fabricated apertures by the dry-transfer method [39] to eliminate the influence from the substrate. As shown in Fig. 2a, successful sample preparation resulted in a hBN flake with a freestanding area larger than 100 μm^2.

During a typical carbon-ion implantation process, a fluence of 2.5×10^6 ions per μm^2 with a 40 keV acceleration energy was applied to achieve a moderate emitter density (around 0.03 cts per μm^2 for sample thickness <10 nm).
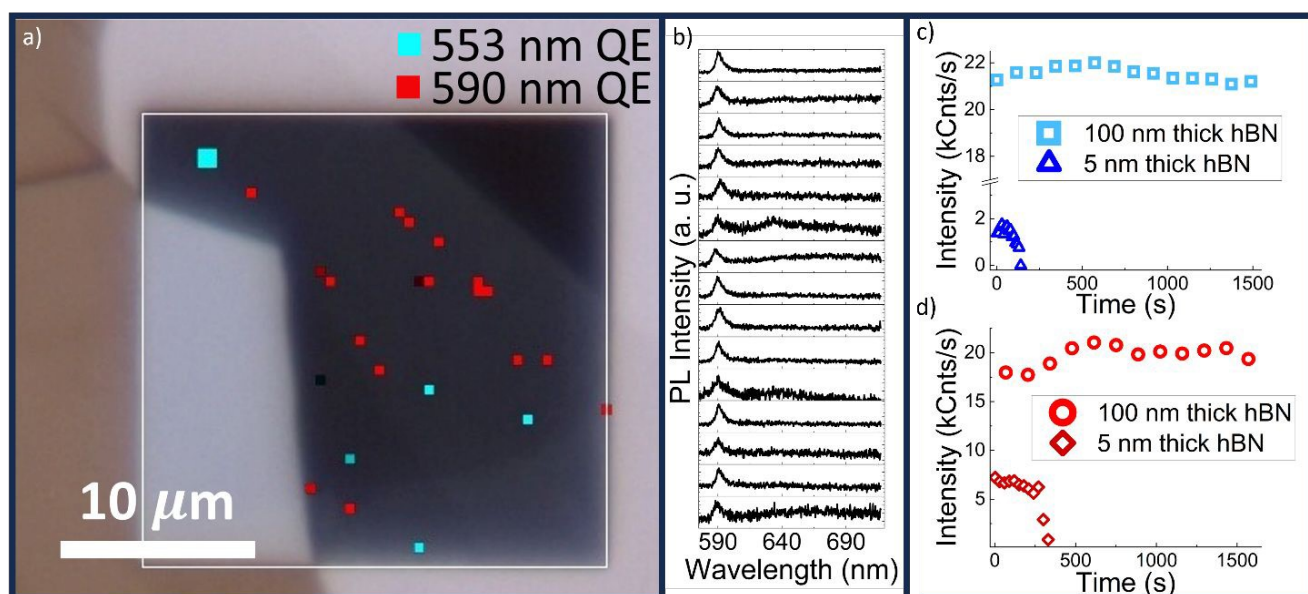

Fig. 2 (a) PL hypermapping of a typical hBN sample. (b) PL spectra of the 590 nm QEs (marked in red) in the map. (c) Typical PL intensity versus time of 553 nm QEs generated in 5 nm (blue triangles) and 100 nm (light blue squares) thick hBN samples. (d) Typical PL intensity versus time of 590 nm QEs generated in 5 nm (maroon diamonds) and 100 nm (red circles) thick hBN samples.

Without applying any post treatment, such as high temperature annealing, preliminary scanning of the samples' PL signal was carried out by a reflective confocal microscope system (detailed in methods). A full photoluminescence (PL) spectrum was acquired at each scanning point, from which the intensities at 553 nm and 590 nm were extracted to generate spatial maps that were then overlaid on the optical image to show emitter distribution. Fig. 2a shows the overlaid map, also called PL intensity hyper-mapping, of a typical hBN flake treated with MCI, revealing localized QEs under 532 nm laser excitation. Most observed QEs can be categorized into two types: one with
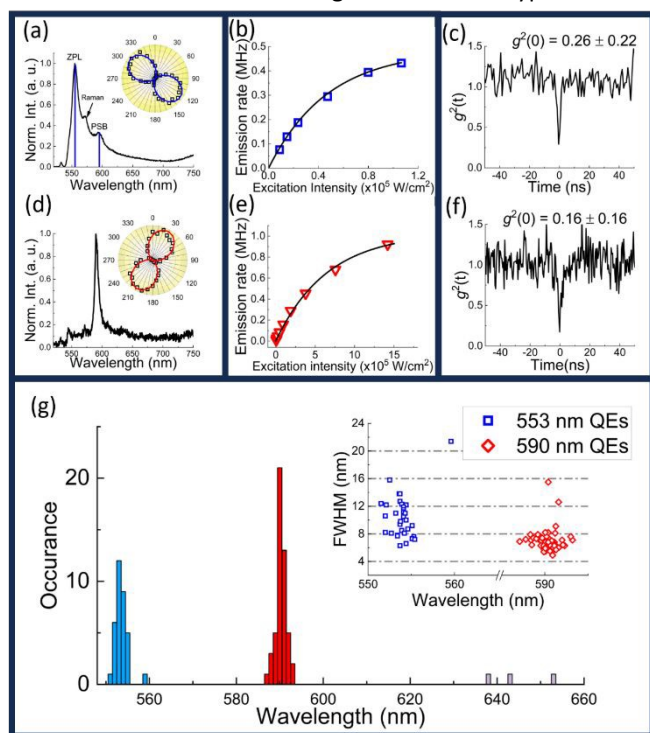

Fig. 3 Optical characterization of the QEs. (a) PL spectrum of a typical 553 nm QE, the insert: PL intensity as a function of the linear polarization angle of the excitation laser. (b) PL intensity as a function of the excitation power for a typical 553 nm QE (c) Photon second-order-correlation function of a typical 553 nm QE. (d) PL spectrum of a typical 590 nm QE, the insert: PL intensity as a function of the linear polarization angle of the excitation laser. (e) PL intensity as a function of the excitation power for a typical 590 nm QE. (f) Photon second order-correlation function of a typical 590 nm QE. (g) Emitters' ZPL wavelength distribution with a bar width of 1 nm. The insert shows the FWHM of the 553 nm (hollow blue triangles) and 590 nm (hollow red diamonds) QEs.

an emission wavelength peaking around 553 nm (coloured in cyan in Fig. 2a) and the other with an emission wavelength peaking around 590 nm (coloured in red in Fig. 2a). For the rest of the paper, these will be denoted as the 553 nm and 590 nm QEs, respectively. The 553 nm QEs were consistent to the recent reported paper by Zhong et al. obtained through carbon ion implantation followed by annealing treatment[37]. The spectra of 590 nm QEs presented in Fig. 2a are plotted in Fig. 2b, demonstrating extraordinary consistency in their spectral profiles.

However, the QEs created in samples with thickness less than 10 nm were generally unstable, with their emission lasting only hundreds of seconds under continuous illumination in ambient

conditions. As illustrated in the plots of PL intensity versus illumination time for 553 nm and 590 nm QEs created in a 5 nm thick hBN sample, shown in Fig. 2c (blue triangles) and Fig. 2d (maroon diamonds), respectively, the emission rates diminished after 120 s and 300 s respectively. Given the small phonon side band (PSB) observed in these QEs, it is reasonable to infer that the defects are mechanically well isolated, with rigid defect structures and an intact surrounding lattice. Meanwhile, some emitters disappeared after months of storage in the air. This is consistent with previous literature which has identified reactions of oxygen with carbonaceous defects in hBN as the source of optical instability in thin flakes (such as 16 monolayers) of hBN [34]. The thin samples result in implantation of defects close to the hBN surface and can result in over penetration, which may leave pores for gas transport. Therefore, the authors concluded that exposing QEs to the environment led to their instability. Since the carbon mask is a separate, free-standing amorphous carbon film used solely to decelerate incoming ions during implantation, it does not play a role in passivating surface defects or mitigating oxygen diffusion as it is not directly coated onto the hBN flakes.

To solve the stability issue, a 50 nm carbon mask over a 100 nm hBN flake sample was selected to achieve a 91.7% stopping efficiency of the carbon ions with negligible over penetration (detailed in supplementary information). After applying MCI to the sample, QEs were created with a total QE areal density of 0.42 cts per μm^2, an order of magnitude higher than the thin samples with identical ion irradiation fluence. The spectral line profiles of the emitters found in thick films match those of the thin films, but with significantly enhanced stability. Typical PL intensity versus time for 553 nm and 590 nm QEs are shown in Fig. 2c (light blue squares) and 2d (red circles) respectively. No brightness degradation was observed for prolonged illumination with long term fluctuations attributed to the drifting of the stage. The population distribution in wavelength of the QEs created in thin and thick samples are almost identical, where 553.5±2.7 nm and 590.7±2.5 nm (Fig. 3g) was obtained from the combined data. Due to fixed acceleration voltage in our current setup, the effect of implantation energy on ZPL distribution was not explored. However, we investigated the influence of fluence and found no notable change in ZPL distribution within the tested fluence range. This may be attributed to the low implanted ion density, where the average spacing between emitters remains larger than their interaction range. Besides 553 nm and 590 nm QEs, other emitters were much less likely (3.4% among the created emitters) to be found in our samples, suggesting the defect creation was dominated by two ultimate processes. As shown in Fig. 3d, the typical spectrum of a 553 nm QE was slightly cut on the short wavelength side as multiple 547 nm long pass filters were used to completely remove the excitation laser light (532 nm CW laser). The sharp feature was still pronounced enough for us to estimate the FWHM to be 10.5±3 nm (43 meV, blue triangles in the insert in Fig. 3g). Besides the Raman signal of hBN, a secondary peak around 596 nm, 161 meV from the ZPL, which is slightly lower than the optical phonon energy of hBN, about

ARTICLE

170 meV [40,41], was observed and has been attributed to the PSB. In contrast, 590nm QEs not only showed a much narrower emission profile and smaller dispersion of FWHM, with a value of 7.1±1.7 nm (25 meV, red diamonds in the insert in Fig. 3g). A PSB at 636 nm (151 meV from the ZPL) was not pronounced except at high excitation laser power. The measured emission linewidths (FWHM) are 25 meV at room temperature ($k_BT \approx$ 25.2 meV) and 7 meV at 87 K ($k_BT \approx$ 7.5 meV), suggesting that the linewidth is predominantly limited by thermal broadening.

QE	τ_r	η	Peak wavelength	FWHM	Dipole
553 nm	1.06±0.48 ns	0.860±0.139	553.5±2.7 nm	10.5 ±3.0 nm	Yes
590 nm	0.69±0.17 ns	0.915±0.078	590.1±2.5 nm	7.1±1.7 nm	Yes

Table 1. Photoluminescence information of the quantum emitters. The values were obtained at room temperature in atmosphere.

Saturation behaviours were observed in both types of QEs with increasing excitation laser power, and the observed maximum emission rates of 553 nm and 590 nm QEs were 0.43 MHz (Fig. 3b) and 0.92 MHz (Fig. 3e) respectively (considered as lower limits, detailed in Method). Although the maximum emission rate of 553 nm QEs is much lower than the 590 nm QEs, they saturate at lower excitation intensity (more than an order of magnitude smaller), suggesting the 533 nm QEs have a larger absorption cross-section. It is also confirmed in the stability data, where PL intensity's long-term fluctuation of the 590 nm QEs was more pronounced as its collecting efficiency is more sensitive to the drifting the stage due to the small spatial dimension responsible for absorption (confirmed below using

The excitation polarization dependence information of the QEs was obtained by rotating the laser's polarization angle, θ, with a half-wave-plate. The data are shown in the inserts inside Fig. 3g for 553 nm and 590 nm respectively, where the QEs'

Fig. 4. STEM-CL intensity mapping of MCI treated 100 nm thick hBN flake. a) Typical mapping of integrated CL intensity (from 547 nm to 563 nm) with the presence of a 553 nm QE (the spectrum was derived by the averaging the bright pixels) and its spectrum showing on the right. b) Typical mapping of integrated CL intensity (from 584 nm to 596 nm) with the presence of a 590 nm QE (circled with cyan dash lines) and its spectrum.

integrated PL emission intensity $I(\theta)$ can be fitted with the function,

$$I(\theta) = I_0 + I_A * \sin^2(\theta - \theta_0), \tag{1}$$

by assuming the linear dipole response for the defects. Here the purity of the dipoles, p was defined as, $p = I_A/(I_A + I_0)$ with a
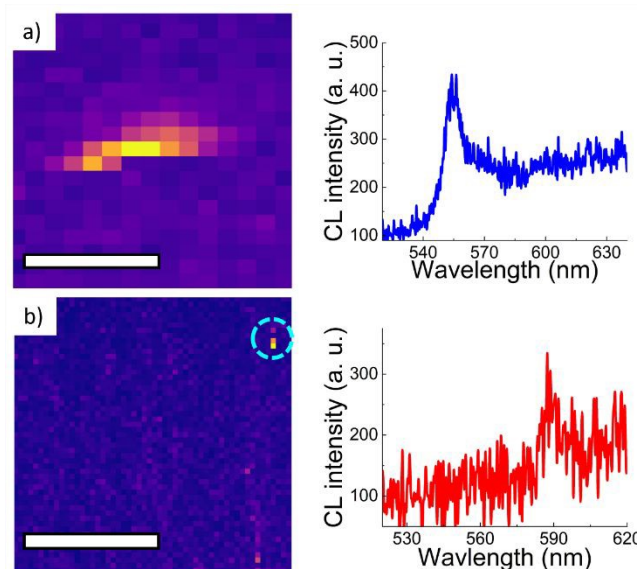
maximum value of 1, where I_0 and I_A denote the base value and the amplitude of the fitting function. According to our data, p value approaching 1 was observed in both types of QEs (typical values of 0.962 and 0.971 were observed in 553 nm and 590 nm QEs). Such observation indicated a single in-plane transition dipole moment was formed between the defects' ground and excited states.

Using a Hanbury-Brown-Twiss (HBT) interferometer, the anti-bunching behaviour originated from the single photon nature of the defects' emission was confirmed (elaborated in the Method section). As shown in Fig. 3c and 3f, $g^2(0)$ values of 0.26±0.22 and 0.16±0.16 were obtained for 553 nm and 590 nm QEs respectively, confirming their single photon emission behaviour with high single photon purity. According to the data, no profound photon bunching at time $\neq 0$ was observed in both types, suggesting the absence of non-radiative shelving state in their electronic states[42]. Therefore the QEs' anti-bunching data was fitted by a background corrected two-level-system model[43],

Nanoscale

Journal Name

ARTICLE

$$g^2(t) = 1 - \eta^2 e^{-|t|/\tau} \qquad (2)$$

$\eta = I_e/(I_e + I_b)$, where I_e and I_b denote the integrated emission intensity and background intensity respectively. τ_r is the defect state's radiative decay mean cycle lifetime, which is the summation of the radiative excitation and decay lifetimes (statistic of the time-resolved data were obtained by fitting the data with Eq. 2. As shown in Table 1, short radiative cycle lifetime was observed for both 553 nm (1.06±0.48 ns) and 590 nm (0.69±0.17 ns) QEs.

nm QEs to electron beams was more than an order of magnitude smaller than that of the 553 nm QEs. This is consistent with the PL measurement, in which photon absorption cross-section of the 590 nm QEs is smaller than that of the 553 nm QEs by a factor of 14, suggesting that the 590 nm QEs are spatially smaller compared to the 553 nm QEs. Therefore, a possible explanation is the 553nm QE's physical size is roughly an order of magnitude bigger than a 590nm QE. As what will be discussed later in the paper, the likelihood of forming multi-carbon defects decreases exponentially as the number of carbon replacement sites increases. It is very unlikely
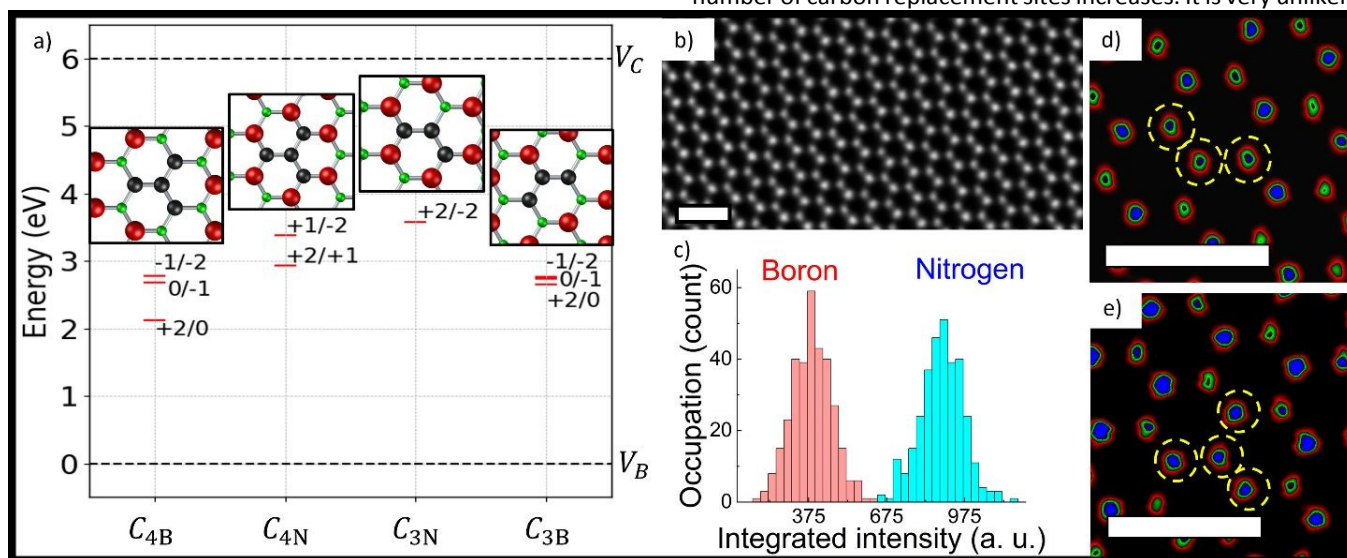

Fig. 5. DFT results and the atomic resolution STEM images of the MCI treated hBN sample. a) Allowed electronic energy states derived from DFT calculation for C_{4B}, C_{4N}, C_{3N} and C_{3B} (from left to right). The inserts show the atomic model of the corresponding defects, where green, black and red spheres denote boron, carbon and nitrogen atoms respectively. b) Typical ADF STEM image of the hBN flake. c) Histogram plot of integrated intensity of each dot in b). d) False colour STEM image of carbon trimer defects C_{3N} replacing "BNB" sites. e) False colour STEM image of carbon tetramer C_{4B} centre at the boron site. All scale bars denote 500 pm. Note DFT calculations have an error margin of ±0.2 eV.

The freestanding sample also allows the characterization of the samples with the scanning transmission electron microscope-cathodoluminescence (STEM-CL) system, where the focused electron beam (e-beam) activates the defect related emission. Fig. 4 shows the CL intensity mapping data collected from a 100 nm thick sample. The CL spectra was obtained by averaging over the bright pixels within the circled areas. According to the data, the CL spectra of the QEs showed identical wavelength and FWHM to their PL versions. Meanwhile, a much higher spatial resolution than the PL data was achieved, where locations of the 553 nm and 590 nm QEs were determined within 50 nm (Fig. 4a) and 4 nm (Fig. 4b) respectively. The radius of the excitation volume introduced by the e-beam, R_e, can be estimated by the empirical equation: $R_e = 1/\rho * (0.0276M * Z^{0.889}) * E_b^{1.67}$ in the unit of μm[44]. Where M is the molar mass (24.8 g/mol), ρ is the density (2.1g/cm³ and Z is the atomic number (mean value of N and B, 6 was applied) of the target material. E_b denotes the energy of the e-beam in keV. For 80 keV acceleration energy, which was used in our experiment, $R_e = 99.5 \, \mu m$ was estimated, which is much bigger than the thickness of the hBN flakes used in our experiment. Therefore, the excitation volume was roughly defined by the size of the e-beam[45], which was much smaller than the size of the observed emission area. So, it is reasonable to consider that the interactive volume of the 590

for the 553nm QE to be giant carbon multimers. A reasonable guess would be the origins of 553nm are clusters of carbon defects that are close to each other[20,46]. Recently Faraon's group reported that carbon defect clusters forming C_B–C_N donor-acceptor pair could potentially be the origins of the observed 553 QEs for in hBN[37]. On the other hand, the 590 nm quantum emitters are most likely attributed to single-defect mechanisms. This distinction can adequately explain the observed differences in ZPL linewidth and PSB strength between the two types of QEs. Besides, the CL data also confirms the low emitter density observed in the PL experiment, as no clusters of the emitters were detected, this further highlights the huge difference between the amount of carbon ions stopped by the flake and the resulting emitter density. Here we use the typical emitter density observed in a 100 nm thick hBN flake, 0.42 cts per μm^2 for analysis as they are stable. Compared to the carbon ions stopped by the flake, 2.5×10^6 per μm^2, an intuitive speculation is more than one carbon atom was required to form an emissive defect.

The subsequent analysis only focuses on the 590 nm QEs as they were more likely to have a single defect configuration. The identity of these single defects, however, is not immediately clear. By assuming the stopping of the carbon ions is a

ARTICLE

completely stochastic process, and the aggregation of carbon ions were negligible, the surface density of n carbon ions replacing neighbouring lattice sites (forming carbon dimers, trimers or tetramers) within a monolayer of hBN, Γ_n can be estimated by evaluating the possible configurations of carbon replacement. Since the concentration of carbon ions in each layer was estimated to be low (<10^{-3}), for each configuration, a lattice site being intact approaches 1. Therefore, Γ_n can be simply written in the form of (detailed in SI):

$$\Gamma_n = \Gamma_s \cdot \sum_{i=1}^{N} \zeta_n \cdot (\Gamma_i \cdot V_{site})^{n-1}, \qquad (3)$$

Here Γ_i denotes the concentration of carbon ions at the ith layer of the hBN flake, which was obtained from the SRIM (The Stopping and Range of Ions in Matter) simulation. V_{site} denotes the average volume occupied by each lattice site. ζ_n denote the number of possible configurations of n carbon ions replacing neighbouring sites. N is the total number of layers of the hBN flake. Γ_s is the effective surface density measured at the implantation target. Γ_s and Γ_i satisfy the relationship: $\Gamma_s = \sum_{i=1}^{N} \Gamma_i = 2.5 \times 10^6$ per μm². According to Eq. 3, the surface density of carbon dimers, trimers, and tetramers were estimated to be 627, 0.185, and 0.000967 per μm², respectively (detailed in SI). Considering the possible aggregation of the carbon ions inside the hBN flake and the self-repairing processes, the actual density was expected to be much higher than the estimation. Suggesting that, most likely, the emissive defects were carbon trimers or tetramers.

We utilize first principles density functional theory (DFT) calculations to further validate the proposed defect structures that might be responsible for the observed emissions at 590 nm. We consider the carbon trimer C_{3B} (replacing NBN sites, left one insert in Fig. 5a) and C_{3N} (replacing BNB sites, left two inset in Fig. 5a) and radial tetramer defects C_{4B} (replacing BN_3 sites, left three inset in Fig. 5a) and C_{4N} (replacing NB_3 sites, left four inset in Fig. 5a) and perform DFT calculations with charged defects to predict the defect transition levels within the band gap. Here we applied the charge defect calculations correction methodology[48] and calculated the charge defect formation energy E_f as a function of the Fermi energy, and the results for C_{4B}, C_{4N}, C_{3N} and C_{3B} are shown in Fig. 5a in the order from left to right (details in SI). The calculated electronic states based on the E_f analysis suggests that C_{4B} has a transition energy 2.1 ± 0.2 eV corresponding to the +2/0 transition, which most closely agrees with the observed emission energy (2.10 eV). However, the calculated energy levels of C_{4N}, C_{3N}, and C_{3B} are approximately 2.9 eV, 3.6 eV, and 2.7 eV, respectively— significantly higher than the observed 2.1 eV and well beyond the typical ±0.2 eV error margin of the applied DFT method (see SI for details).

To corroborate the DFT prediction, atomic resolution STEM images of the samples were taken to reveal the atomic structures involved in the emission. A typical annular dark field (ADF) image of the MCI hBN sample taken over the emitter sites is shown in Fig. 5b, where the hexagonal structure of boron

nitride was identified. The image was taken along the direction perpendicular to the flake plane. Here, the hBN crystals used in our experiment showed AA' stacking, where boron and nitrogen sites were alternatively stacking on each other between layers. In such a configuration, two adjacent layers form columns of atoms with identical total Z value, resulting in no contrast difference. Thus, for flakes with an even number of layers, the lattice sites exhibit identical intensity. In contrast, for flakes with an odd number of layers, the intensity difference between boron and nitrogen sites of the non-compensated monolayer is retained. Therefore, Fig. 5b were taken from an odd layer hBN flake, where the boron (dimmer) and nitrogen (brighter) sites can be well distinguished. A statistical analysis is shown in Fig. 5c, where the histogram of the integrated intensity for each lattice site in Fig. 5b (the image shown was cropped to a quarter of the original one to match the scale) was plotted, showing unambiguous difference between the boron and nitrogen sites. Therefore, lattice sites with ADF image intensity in between the nitrogen and boron sites were attributed to carbon replacement ($Z = 6$). As shown in Fig. 5d and 5e, where carbon trimer, replacing BNB sites and carbon tetramer replacing BN_3 sites (marked with yellow dashed circles) were observed respectively. The data suggested that C_{4B} did form during the MCI process, supporting the emitter density analysis and DFT calculations.

Conclusions

MCI enables repeatable deterministic production of bright, stable and atom-like room temperature QEs in hBN, ensuring a highly consistent yield of QEs with excellent single photon purity. The mask approach is also inherently amenable to lithography, meaning it is consistent with the ability to place QEs deterministically in space. Our research is both technological and scientific interest, as it provides consistent reproducible QE sample production, allowing reliable platform for characterization and fabrication research. According to our data, boron centred carbon tetramers, C_{4B} were suggested to be the origins of the 590 nm QEs, while the 553 nm QEs are attributed to the donor-acceptor pairs induced by carbon-defect clusters. The QEs produced with this method exhibiting exceptional stability, underlining the robustness of the proposed approach. Such reliability is paramount when considering the demands of any practical applications, especially the industrial-scale production, where reproducibility and consistency are central to achieving standardized outputs, potentially introducing a transformative dimension to the landscape of quantum technology.

Author contributions

Conceptualization: MH, JW

Methodology: MH, JW, WC

Investigation: MH, HH, WC, JW

ARTICLE

Conflicts of interest

There are no conflicts to declare.

Data availability

All data will be available at Deterministic Fabrication of Highly Reproducible Monochromatic Quantum Emitters in Hexagonal Boron Nitride (https://zenodo.org/records/15233137).

Acknowledgements

References

1   N. Y. Yao, L. Jiang, A. V. Gorshkov, P. C. Maurer, G. Giedke, J. I. Cirac and M. D. Lukin, *Nature Communications*, 2012, **3**, 800.

2   T. van der Sar, Z. H. Wang, M. S. Blok, H. Bernien, T. H. Taminiau, D. M. Toyli, D. A. Lidar, D. D. Awschalom, R. Hanson and V. V. Dobrovitski, *Nature*, 2012, **484**, 82–86.

3   H. Bernien, B. Hensen, W. Pfaff, G. Koolstra, M. S. Blok, L. Robledo, T. H. Taminiau, M. Markham, D. J. Twitchen, L. Childress and R. Hanson, *Nature*, 2013, **497**, 86–90.

4   G. Waldherr, Y. Wang, S. Zaiser, M. Jamali, T. Schulte-Herbrüggen, H. Abe, T. Ohshima, J. Isoya, J. F. Du, P. Neumann and J. Wrachtrup, *Nature*, 2014, **506**, 204–207.

5   B. Hensen, H. Bernien, A. E. Dréau, A. Reiserer, N. Kalb, M. S. Blok, J. Ruitenberg, R. F. L. Vermeulen, R. N. Schouten, C. Abellán, W. Amaya, V. Pruneri, M. W. Mitchell, M. Markham, D. J. Twitchen, D. Elkouss, S. Wehner, T. H. Taminiau and R. Hanson, *Nature*, 2015, **526**, 682–686.

6   C. E. Bradley, J. Randall, M. H. Abobeih, R. C. Berrevoets, M. J. Degen, M. A. Bakker, M. Markham, D. J. Twitchen and T. H. Taminiau, *Phys. Rev. X*, 2019, **9**, 031045.

7   X. Zhou, X. Li, Q. Chen, G. Koolstra, G. Yang, B. Dizdar, Y. Huang, C. S. Wang, X. Han, X. Zhang, D. I. Schuster and D. Jin, *Nature Physics*, 2024, **20**, 116–122.

8   S. Noda, A. Chutinan and M. Imada, *Nature*, 2000, **407**, 608–610.

9   R. Raussendorf, D. E. Browne and H. J. Briegel, *Phys. Rev. A*, 2003, **68**, 022312.

10 R. Raussendorf, S. Bravyi and J. Harrington, *Phys. Rev. A*, 2005, **71**, 062313.

11 N. Coste, D. A. Fioretto, N. Belabas, S. C. Wein, P. Hilaire, R. Frantzeskakis, M. Gundin, B. Goes, N. Somaschi, M. Morassi, A. Lemaître, I. Sagnes, A. Harouri, S. E. Economou, A. Auffeves, O. Krebs, L. Lanco and P. Senellart, *Nature Photonics*, 2023, **17**, 582–587.

12 A. Lohrmann, N. Iwamoto, Z. Bodrog, S. Castelletto, T. Ohshima, T. J. Karle, A. Gali, S. Prawer, J. C. McCallum and B. C. Johnson, *Nature Communications*, 2015, **6**, 7783.

13 Y. Zhou, Z. Wang, A. Rasmita, S. Kim, A. Berhane, Z. Bodrog, G. Adamo, A. Gali, I. Aharonovich and W. Gao, *Science Advances*, 2018, **4**, eaar3580.

14 J. Wang, Y. Zhou, Z. Wang, A. Rasmita, J. Yang, X. Li, H. J. von Bardeleben and W. Gao, *Nature Communications*, 2018, **9**, 4106.

15 W. Liu, V. Ivanov, K. Jhuria, Q. Ji, A. Persaud, W. Redjem, J. Simoni, Y. Zhiyenbayev, B. Kante, J. G. Lopez, L. Z. Tan and T. Schenkel, *Phys. Rev. Appl.*, 2023, **20**, 014058.

16 H. I. Rasool, C. Ophus and A. Zettl, *Advanced Materials*, 2015, **27**, 5771–5777.

17 C. Chakraborty, L. Kinnischtzke, K. M. Goodfellow, R. Beams and A. N. Vamivakas, *Nature Nanotechnology*, 2015, **10**, 507–511.

18 G. Grosso, H. Moon, B. Lienhard, S. Ali, D. K. Efetov, M. M. Furchi, P. Jarillo-Herrero, M. J. Ford, I. Aharonovich and D. Englund, *Nature Communications*, 2017, **8**, 705.

19 S. Roy, X. Zhang, A. B. Puthirath, A. Meiyazhagan, S. Bhattacharyya, M. M. Rahman, G. Babu, S. Susarla, S. K. Saju, M. K. Tran, L. M. Sassi, M. A. S. R. Saadi, J. Lai, O. Sahin, S. M. Sajadi, B. Dharmarajan, D. Salpekar, N. Chakingal, A. Baburaj, X. Shuai, A. Adumbumkulath, K. A. Miller, J. M. Gayle, A. Ajnsztajn, T. Prasankumar, V. V. J. Harikrishnan, V. Ojha, H. Kannan, A. Z. Khater, Z. Zhu, S. A. Iyengar, P. A. da S. Autreto, E. F. Oliveira, G. Gao, A. G. Birdwell, M. R. Neupane, T. G. Ivanov, J. Taha-Tijerina, R. M. Yadav, S. Arepalli, R. Vajtai and P. M. Ajayan, *Advanced Materials*, 2021, **33**, 2101589.

20 Q. Tan, J.-M. Lai, X.-L. Liu, D. Guo, Y. Xue, X. Dou, B.-Q. Sun, H.-X. Deng, P.-H. Tan, I. Aharonovich, W. Gao and J. Zhang, *Nano Letters*, 2022, **22**, 1331–1337.

21 S. Li, G. Thiering, P. Udvarhelyi, V. Ivády and A. Gali, *Nature Communications*, 2022, **13**, 1210.

22 Z. Benedek, R. Babar, Á. Ganyecz, T. Szilvási, Ö. Legeza, G. Barcza and V. Ivády, *npj Computational Materials*, 2023, **9**, 187.

23 Y.-M. He, G. Clark, J. R. Schaibley, Y. He, M.-C. Chen, Y.-J. Wei, X. Ding, Q. Zhang, W. Yao, X. Xu, C.-Y. Lu and J.-W. Pan, *Nature Nanotechnology*, 2015, **10**, 497–502.

24 T. T. Tran, K. Bray, M. J. Ford, M. Toth and I. Aharonovich, *Nature Nanotechnology*, 2016, **11**, 37–41.

25 J. Ziegler, R. Klaiss, A. Blaikie, D. Miller, V. R. Horowitz and B. J. Alemán, *Nano Lett.*, 2019, **19**, 2121–2127.

26 X. Xu, Z. O. Martin, D. Sychev, A. S. Lagutchev, Y. P. Chen, T. Taniguchi, K. Watanabe, V. M. Shalaev and A. Boltasseva, *Nano Letters*, 2021, **21**, 8182–8189.

27 A. B. D. Shaik and P. Palla, *Sci Rep*, 2021, **11**, 12285.

28 S. J. U. White, T. Yang, N. Dontschuk, C. Li, Z.-Q. Xu, M. Kianinia, A. Stacey, M. Toth and I. Aharonovich, *Light: Science & Applications*, 2022, **11**, 186.

29 S. A. Tawfik, S. Ali, M. Fronzi, M. Kianinia, T. T. Tran, C. Stampfl, I. Aharonovich, M. Toth and M. J. Ford, *Nanoscale*, 2017, **9**, 13575–13582.

30 B. Shevitski, S. M. Gilbert, C. T. Chen, C. Kastl, E. S. Barnard, E. Wong, D. F. Ogletree, K. Watanabe, T. Taniguchi, A. Zettl and S. Aloni, *Phys. Rev. B*, 2019, **100**, 155419.

Nanoscale Accepted Manuscript

31   D. Mendelson Noahand Chugh, J. R. Reimers, T. S. Cheng, A. Gottscholl, H. Long, C. J. Mellor, A. Zettl, V. Dyakonov, P. H. Beton, S. V. Novikov, C. Jagadish, H. H. Tan, M. J. Ford, M. Toth, C. Bradac and I. Aharonovich, *Nature Materials*, 2016, **20**, 321–328.

32   N. R. Jungwirth and G. D. Fuchs, *Phys. Rev. Lett.*, 2017, **119**, 057401.

33   F. Hayee, L. Yu, J. L. Zhang, C. J. Ciccarino, M. Nguyen, A. F. Marshall, I. Aharonovich, J. Vučković, P. Narang, T. F. Heinz and J. A. Dionne, *Nature Materials*, 2020, **19**, 534–539.

34   K. Li, T. J. Smart and Y. Ping, *Phys. Rev. Mater.*, 2022, **6**, L042201.

35   Y. Chen, A. Gale, K. Yamamura, J. Horder, A. Condos, K. Watanabe, T. Taniguchi, M. Toth and I. Aharonovich, *Applied Physics Letters*, 2023, **123**, 041902.

36   S. Sarkar, Y. Xu, S. Mathew, M. Lal, J.-Y. Chung, H. Y. Lee, K. Watanabe, T. Taniguchi, T. Venkatesan and S. Gradečak, *Nano Letters*, 2024, **24**, 43–50.

37   D. Zhong, S. Gao, M. Saccone, J. R. Greer, M. Bernardi, S. Nadj-Perge and A. Faraon, *Nano Lett.*, 2024, **24**, 1106–1113.

38   J. F. Ziegler, M. D. Ziegler and J. P. Biersack, *Nuclear Instruments and Methods in Physics Research Section B: Beam Interactions with Materials and Atoms*, 2010, **268**, 1818–1823.

39   A. Castellanos-Gomez, M. Buscema, R. Molenaar, V. Singh, L. Janssen, H. S. J. van der Zant and G. A. Steele, *2D Materials*, 2014, **1**, 011002.

40   S. Reich, A. C. Ferrari, R. Arenal, A. Loiseau, I. Bello and J. Robertson, *Phys. Rev. B*, 2005, **71**, 205201.

41   H. I. Røst, S. P. Cooil, A. C. Åsland, J. Hu, A. Ali, T. Taniguchi, K. Watanabe, B. D. Belle, B. Holst, J. T. Sadowski, F. Mazzola and J. W. Wells, *Nano Letters*, 2023, **23**, 7539–7545.

42   P. Michler, A. Imamoğlu, M. D. Mason, P. J. Carson, G. F. Strouse and S. K. Buratto, *Nature*, 2000, **406**, 968–970.

43   R. Brouri, A. Beveratos, J.-P. Poizat and P. Grangier, *Opt. Lett.*, 2000, **25**, 1294–1296.

44   K. Kanaya and S. Okayama, *Journal of Physics D-Applied Physics*, 1972, **5**, 43-.

45   B. G. Yacobi and D. B. Holt, *Cathodoluminescence Microscopy of Inorganic Solids*, Springer US, New York, 1990.

46   C. Freysoldt and J. Neugebauer, *Physical Review B*, 2018, **97**, 205425.

Nanoscale Accepted Manuscript

Data in the article: "Deterministic Fabrication of Highly Reproducible Monochromatic Quantum Emitters in Hexagonal Boron Nitride", can be found below:

https://zenodo.org/records/15233137